



**HAL**  
open science

## Coupled meso-macro simulation of woven fabric local deformation during draping

Akira Iwata, Takuya Inoue, Naïm Naouar, Philippe Boisse, Stepan Lomov

► **To cite this version:**

Akira Iwata, Takuya Inoue, Naïm Naouar, Philippe Boisse, Stepan Lomov. Coupled meso-macro simulation of woven fabric local deformation during draping. *Composites Part A: Applied Science and Manufacturing*, 2019, 118, pp.267-280. 10.1016/j.compositesa.2019.01.004 . hal-02288957

**HAL Id: hal-02288957**

**<https://hal.science/hal-02288957v1>**

Submitted on 10 Oct 2024

**HAL** is a multi-disciplinary open access archive for the deposit and dissemination of scientific research documents, whether they are published or not. The documents may come from teaching and research institutions in France or abroad, or from public or private research centers.

L'archive ouverte pluridisciplinaire **HAL**, est destinée au dépôt et à la diffusion de documents scientifiques de niveau recherche, publiés ou non, émanant des établissements d'enseignement et de recherche français ou étrangers, des laboratoires publics ou privés.



Distributed under a Creative Commons Attribution - NonCommercial 4.0 International License

# Coupled meso-macro simulation of woven fabric local deformation during draping

Akira Iwata<sup>a</sup>, Takuya Inoue<sup>a</sup>, Naim Naouar<sup>b</sup>, Philippe Boisse<sup>b</sup>, Stepan V. Lomov<sup>c,\*</sup>

<sup>a</sup> Engineering Development Center, Toray Industries, Inc., 3-1 Sonoyama 3-chome, Ostu, Shiga 520-0842, Japan

<sup>b</sup> Université de Lyon, LaMCoS, INSA Lyon, Av. Jean Capelle, F69621 Villeurbanne, France

<sup>c</sup> Department of Materials Engineering, KU Leuven, Kasteelpark Arenberg 44, BE-3001 Leuven, Belgium

The prediction of yarn buckling and distortions require detailed modelling of the fabric and yarns deformations on the meso-level (level of the interlacing structure). In the current research, computationally viable meso-level simulation is achieved by coupling continuous macro draping simulation with a local meso-modeling in the location where the defects are expected to occur. The macro-simulation uses a membrane-shell continuous model of the fabric. A hyperelastic constitutive model for the yarns (Charmetant – Boisse) is used in the meso-modelling. The model parameters are identified and validated in independent tension, shear, compaction and bending tests of the yarn and the fabric. The simulation reproduces local yarn slippage and buckling, e.g., the yarn distortion on the 3D mould corner. The simulations are compared with the local fabric distortions observed during draping experiments for two carbon plain weave fabrics (12K carbon-fibre tows and with spread tows) on a hemispherical and on a box-shaped moulds.

## 1. Introduction

Several defects can occur during draping of a textile reinforcement over a mould. Wrinkling, the most severe of these defects, can be detected in continuous simulations of the draping process, see the recent review [1]. Apart from the wrinkling, yarn buckling and distortions of the yarn interlacing during draping can be of serious consequence for the local properties of the consolidated composite part and affect its load-carrying ability. During draping of a reinforcement fabric over a 3D mould there always exist “problem” locations: e.g., corners, edges, double-curvature spots, regions of high curvature, and negative curvature. Whether such a location creates a problem also depends on the stresses and especially on the tensions. The preform deformation in the regions of “easy” draping, low-to-medium curvature can be simulated with good precision in draping simulations, if an appropriate and sufficiently detailed constitutive model of the fabric is used. This prediction includes local fabric shear and wrinkling. When it comes to the “problem” locations, then the main assumption of the draping simulations, namely that the preform can be considered as a membrane/shell with certain continuous laws of the shear, tension and bending/torsion deformation resistance, loses its validity – just because the radii of curvature become comparable with the structural scales of the reinforcement – yarn spacing and yarn width. This situation asks for

modelling to be on the meso-scale, i.e., replacement of a continuous description of the preform with the detailed structure of the yarns interlacing in the preform, accounting for differences in the local deformation conditions. Such simulations cannot be reduced to meso-simulations of a textile unit cell. The latter normally assumes periodic boundary conditions and is suitable for identification of the macro-scale fabric constitutive laws based on meso-scale fabric structure and yarns behaviour [2–4], rather than for modelling of the local fibrous structure distortions, which by definition are not periodic.

The last decade saw an advent of modelling of macro-scale draping problems with full representation of all yarns in the fabric, which can be labelled “large scale meso”: meso-scale models which go beyond a unit cell representation of a textile structure. These are models on non-crimp (multi-layered warp-knit stitched) fabrics [5,6], braids [7] and woven fabrics [8]. Large-scale meso-models are, of course, the most representative; they, however, naturally demand significant computational resources and require days of calculations even on CPU clusters, which can be prohibitive for their practical use for the draping strategies selection.

A way to handle the computational enormity of a large scale meso-problem can be the introduction of local modelling on the meso-scale, i.e., replacement of a continuous description of the preform with the detailed structure of the yarns interlacing in the preform at certain

\* Corresponding author.

E-mail address: [stepan.lomov@kuleuven.be](mailto:stepan.lomov@kuleuven.be) (S.V. Lomov).

locations, with the boundary conditions for the meso-problem taken from the local strain state predicted by the macro-model. The authors will nickname such an approach a “macro-meso zoom” (MMZ) calculation. Such simulations were proposed as a general approach for solid mechanics [9–12], mechanics of heterogeneous media [13,14], were used for modelling of consolidated composites (see the pioneering work [15] and a general description of the approach in [16]). To the authors’ knowledge, the MMZ modelling has not yet been attempted for forming problems, most probably due to the complexity of the nonlinear material models.

This paper presents a demonstration of the MMZ simulation for two plain-weave carbon fabrics, very different in their parameters: one fabric is woven of conventional 12 K carbon tows, whilst the other contains spread 12 K tows, which leads to a difference of the fabrics’ areal density of more than two times. Therefore, apart from the proof-of-concept of the macro-meso-zoom draping simulations, the presented experimental results and the simulations may be of interest in view of the importance of thin ply laminate design [17]. The MMZ numerical simulations use membrane – shell representation of the nonlinear fabric constitutive behaviour in the macro-simulation [18,19], and Charnant – Boisse hyperelastic model [20] for the yarns in meso-analysis; the fabric geometrical models are created with WiseTex [21,22]. The calculated local distortions of the yarns are compared with the experimental observations for draping on a hemispherical and a box-shaped moulds.

## 2. Fabrics and moulds. Draping experiments

Table 1 shows parameters of carbon-fibre fabrics used in experiments and in the modelling. A geometrical model of the fabric, shown in Table 1, was created using WiseTex software [21] and transferred to Abaqus/Explicit as described by Lomov et al [22]. This model was the basis for the meso-model comprising several unit cells. The parameters of the model (ends/picks count, yarn width and thickness) are as shown in Table 1; the fabrics are balanced, hence the crimp of the warp and the weft is the same; the yarn cross section shape was assumed to be elliptical. The WiseTex geometrical model has certain yarn interpenetrations, which were handled by solving the contact problem in Abaqus/Explicit.

The draping experiments (see Fig. 1a) were performed as follows. After the fabric was placed over the mould with fixed corner points, where the fabric is fixed with double-sided tape (cf. images of the Fabric A after the draping in Fig. 2), the acrylic plate over the fabric was moved down with steps of 10 mm, and the fabric deformation at each step was captured with a camera. The moulds, a hemispherical (radius 60 mm) and a box-shaped (four different radii of the corners, 10, 20, 30 and 40 mm) are shown in Fig. 1b, c.

The aim of the test was to provide information of the local deformations of the Fabric and the yarns. The typical results of the tests are shown in Fig. 2. The characteristic local distortions of the yarn are the yarn buckling and slippage of the yarn. These distortions are more evident for Fabric B.

The yarn buckling is out-of-plane. When compressed and impregnated, these buckles will be flattened, leading to the local severe fibre misalignment, thereby downgrading the local stiffness and the strength of the composite. Yarn slippage creates wide gaps between the yarns, which will become resin-rich pockets in the impregnated composite. Such pockets can be initiation sites for matrix cracking, as this is the case with non-crimp fabrics [23,24].

Fabrics A and B have very different yarn widths: spread yarns in Fabric B are 2.5 times wider than in Fabric A, and almost three times thinner; accordingly, areal density of Fabric B is 2.3 times lower than that of Fabric A. The local distortions behaviour of the two fabrics reflects this difference in their architecture.

Fig. 2a shows forming test results on the hemispherical mould. Fabric A can be formed without local distortions such as yarn buckling and yarn slippage. Fabric A consists of non-spread yarns with relatively large crimp and high areal density of fabric, which means that the binding force between yarns is sufficiently strong to prevent yarn slippage. The absence of yarn buckling can be attributed to the small width of the yarns (3 mm, see Table 1) and to their crimp. Yarns between the woven intersections have to accommodate the mould curvature; on a small distance this accommodation means small displacement of the crimp interval ends; the associated buckling is “absorbed” by the already existing crimp of the yarn. On the other hand, Fabric B consists of spread yarns with small crimp and low areal density. As shown in Fig. 2a, Fabric B forms clear local distortions during draping on the hemispherical mould, which are mainly yarn buckling. The

**Table 1**  
Fabric parameters.

Parameter	Fabric A	Fabric B
<i>Specified in the data sheet</i>		
Yarn and fibre type	Carbon T700S 12K	Carbon T700S 12K spread
Weave	Plain	Plain
Ends and picks count, yarns/cm	2.95	1.28
Areal density, g/m <sup>2</sup>	480	210
<i>Measured</i>		
Yarn width, mm	3.00	6.75
Yarn thickness, mm	0.323	0.126
Crimp, %	0.6%	< 0.1%
Fabric image		
WiseTex model		

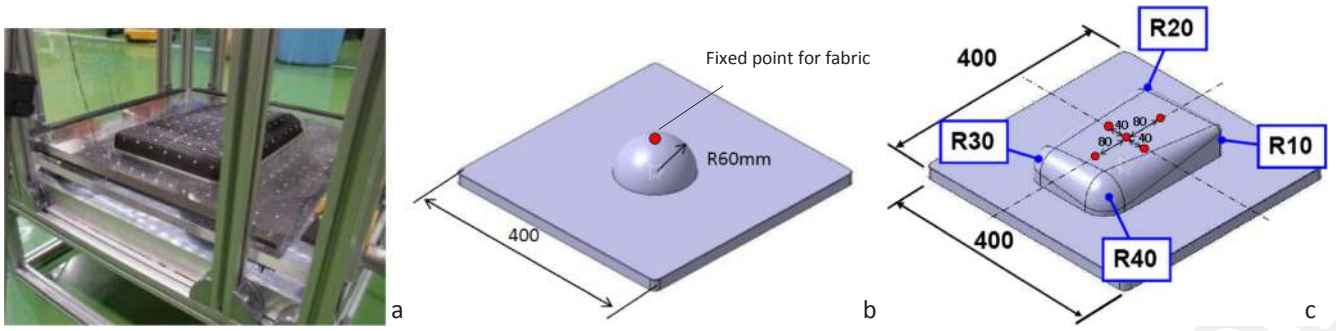


Fig. 1. The draping experiment: (a) setup, moulds: (b) hemispherical; (c) box-shape. (For interpretation of the references to colour in this figure legend, the reader is referred to the web version of this article.)

buckling is possibly a result of the impossibility of the relatively large (yarn width of 6.75 mm, see Table 1) flat (because of low crimp) elements of the fabric to conform to the curvature of the mould. Noticeably the local buckling happens in the regions of low shear angle of the fabric, where the main deformation mode is the yarn bending rather than shear and lateral compression. The buckling zone is a zone where the yarns are in transition from one high shear region to another. The yarns are constrained laterally, hence elongation of the yarns, prescribed by their out-of-plane movement during draping, cannot be freely compensated by their shear. Hence the yarns are forced to deviate from the fabric surface thereby creating a buckle. Harrison et al [25] have noticed the same phenomenon of buckling promoted by wider yarns.

Fig. 2b shows forming test results on the box-shaped mould. Fabric A can be formed without local distortions in spite of high curvature of the corners. Of course, micro slippage and buckling of yarn could occur, but clear local distortions are not seen. On the other hand, the Fabric B develops yarn slippage and yarn buckling on the corners of the box. The buckling is explained by the same factors as with the hemisphere (intensified because of higher curvature). Yarn slippage and the creation of gaps between the yarns is explained by the need for the fabric to accommodate the increased width occupied by a given number of yarns over the surface of the mould in comparison with the corresponding width in the flat fabric. The same number of yarns has to be distributed over increased width. With the high crimp and the high areal density of Fabric A, the slippage is resisted by the friction forces between yarns. The width increase is forced to redistribute over number of yarns, which is high enough to create no noticeable gaps. In flat Fabric B, the yarns are not well fixed in their positions and slip easily; the width increase is hence accommodated locally and a gap is created.

The MMZ simulation in the present paper reproduces the buckling and splitting modes of the yarn distortion on the two moulds and the observed differences between the behaviour of the two fabrics.

### 3. Constitutive models and the identifying experiments

#### 3.1. Constitutive model for the fabric

The macro-draping model, proposed by Nishii et al. [18,19], was implemented in ABAQUS/Explicit. The model utilises the membrane – shells description of the fabric, with a membrane responsible for the in-plane deformation resistance (tension and shear) and two offset shells defining the bending resistance of the fabric (see the schematics in Fig. 3). The parameters of the model are defined as follows:

- Membrane: tension and shear resistance as defined by the experimentally measured curves (Fig. 4). Coupling between tensile and shear behaviour [26,27] is not taken into account in the present simulations.
- Offset shell: Young’s modulus is calculated as

$$E_{shell} = B_f \frac{48}{t(48d^2 + t^2)}$$

where  $E_{shell}$  is Young’s modulus of shell,  $B_f$  is bending stiffness of fabric,  $t$  is thickness of Fabric and  $d$  is offset distance of shell.

The model was identified in uniaxial-tension, bias-extension and bending tests of the Fabric As follows (the equivalence of the warp and weft direction tension and bending deformation resistance for was checked experimentally and the difference was found to lie well within the data scatter).

Uniaxial tension tests were done using the method described in [28,29]; The gauge length of specimens was 50 mm and the width of specimens depended on a type of fabric: for Fabric A, the width was selected such that the specimens contain 8 warp yarns; for Fabric B the number of yarns was 5. The test setup and typical stress-strain curve are shown in Fig. 4a. The lower stiffness of Fabric A may be explained by its higher crimp.

Bias extension tests were done for identifying shear parameters for the macro-draping simulation, as described, for example, in [30]. The bias-extension setup and test results are shown in Fig. 4b. The shear tests were done up to appearance of wrinkling; the curves used for the calculations were linearly extrapolated (as shown in Fig. 4b). Fabric B has much higher (100 times higher shear resistance) shear deformability than Fabric A, indicating easier movement of yarns in Fabric B.

The cantilever test [1,31] was applied to identify the bending parameters. The test setup and test results are shown in Fig. 4c. Fabric A has about two times higher bending stiffness than Fabric B, which may be explained by higher weaving density of Fabric A and its higher crimp, as theorised in [32].

Friction coefficient tool-fabric of 0.2 was identified using KES-F equipment.

#### 3.2. Constitutive model for the yarns

For the yarns, the hyperelastic model of Charmetant-Boisse [20] was used. The yarn is assumed to be a transversely isotropic material.  $\underline{G}_1$  is the unit vector in the fiber direction and  $\underline{G}_1 = \underline{G}_1 \otimes \underline{G}_1$  the associated structural tensor. The second Piola – Kirchhoff stress tensor  $\underline{S}$  derives from a potential  $w$  of the Cauchy–Green deformation tensor  $\underline{C}$  which, in the case of transverse isotropic materials, depends on the following invariants [33,34]:

$$\underline{S} = 2 \frac{\partial w}{\partial \underline{C}} \quad w = w(Tr(\underline{C}), Tr(\underline{C}^2), Det(\underline{C}), Tr(\underline{C} \cdot \underline{G}_1), Tr(\underline{C}^2 \cdot \underline{G}_1)) \quad (a)$$

In the case of a yarn made of parallel fibres the potential  $w$  was written as a function of the invariant of elongation  $I_{elong}$ , compaction  $I_{comp}$ , distortion  $I_{dist}$  and longitudinal shear  $I_{cis}$ . These invariants, called ‘physical invariants’ are used because they represent the deformation modes of the yarn and because they are measured during identification tests. Their relation with the invariants of Eq. (a) are summarised in Table 3. The stress  $\underline{S}$  is derived from the potential  $w$  in which the

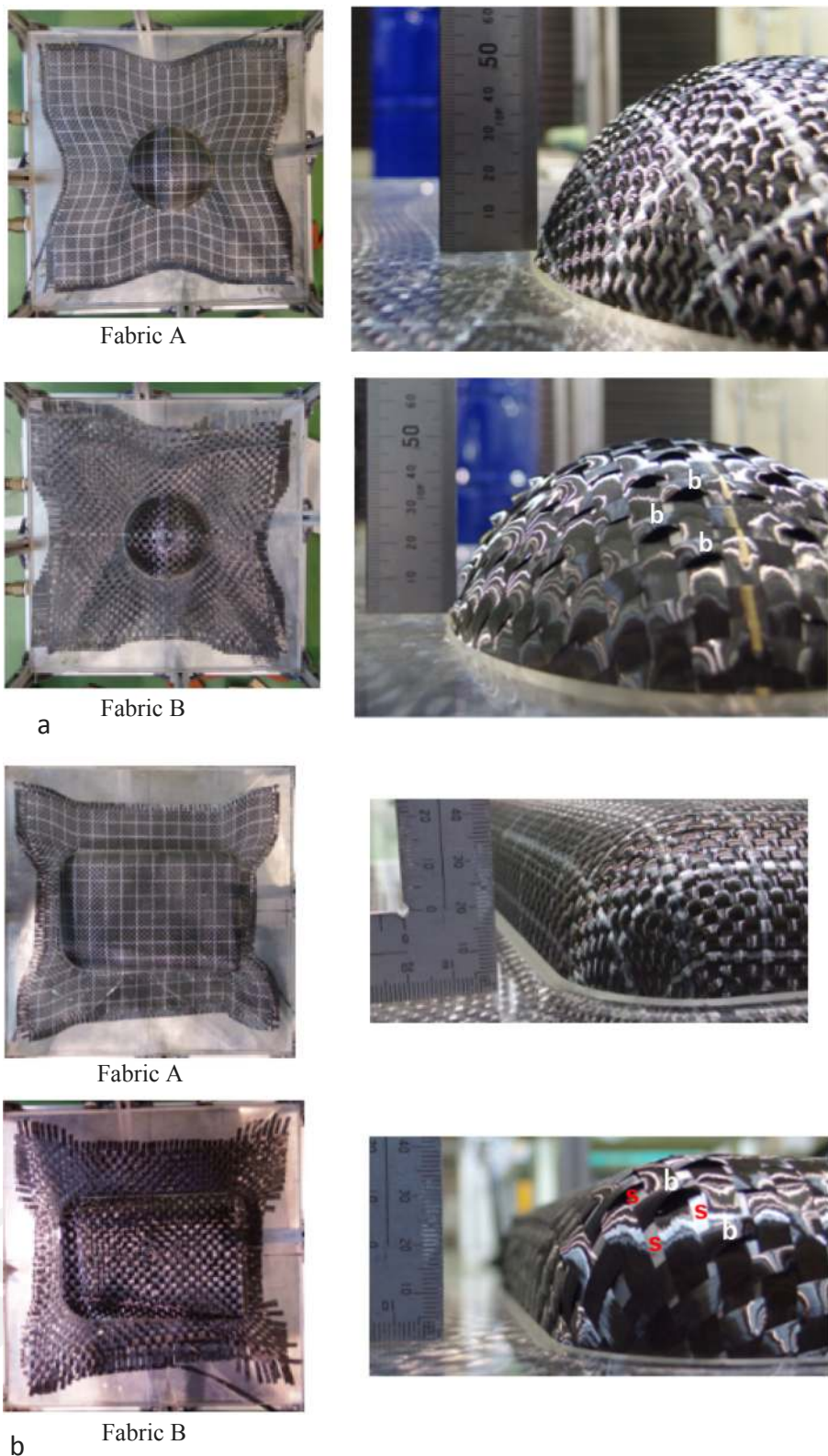


**Fig. 2.** Typical results of the draping tests: (a) hemispherical mould; (b) box-shaped mould. Local yarns distortions: **b** – buckling, **s** – slippage. (For interpretation of the references to colour in this figure legend, the reader is referred to the web version of this article.)

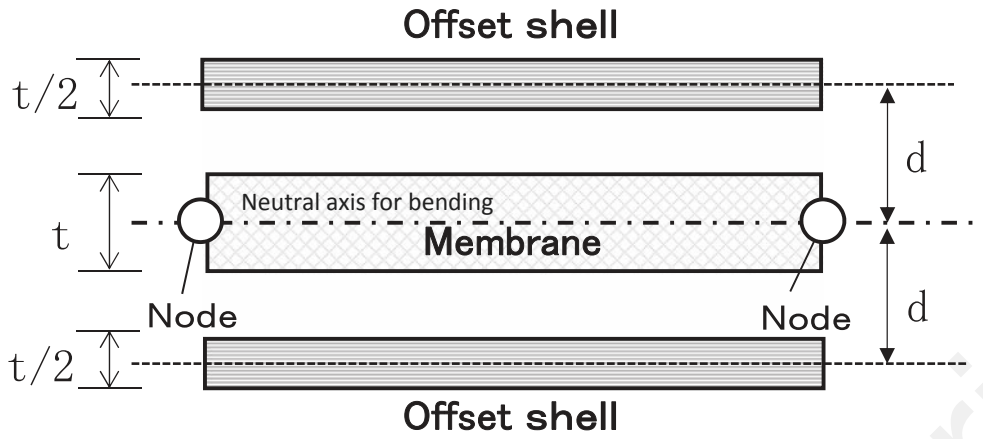
contributions of each deformation mode are decoupled:

$$w_{total} = w_{elong}(I_{elong}) + w_{comp}(I_{comp}) + w_{dist}(I_{dist}) + w_{cis}(I_{cis})$$

$$\underline{\underline{S}}_{total} = 2 \left( \frac{\partial w_{elong}}{\partial I_{elong}} \frac{\partial I_{elong}}{\partial \underline{\underline{C}}} + \frac{\partial w_{comp}}{\partial I_{comp}} \frac{\partial I_{comp}}{\partial \underline{\underline{C}}} + \frac{\partial w_{dist}}{\partial I_{dist}} \frac{\partial I_{dist}}{\partial \underline{\underline{C}}} + \frac{\partial w_{cis}}{\partial I_{cis}} \frac{\partial I_{cis}}{\partial \underline{\underline{C}}} \right) \quad (b)$$

(c)

The hyperelastic constitutive law is determined when the potentials



✂ Two offset shell and membrane share same nodes

Fig. 3. Schematics of the fabric constitutive model [18,19].

of extension  $w_{elong}$ , compaction  $w_{comp}$ , distortion  $w_{dist}$  and shear  $w_{cis}$  are fixed. They are chosen according to the experimental tests and for convexity reasons. The potentials used in the present work and parameters identified for Fabric A and B are given in Table 2. The reader is referred to [35] for detailed description of these deformation modes.

These parameters, which are related to elongation, compression, distortion and longitudinal shear on a single yarn, were identified by experiments and simulations as follows.

**Elongation** parameters are directly identified from the tensile test of single yarns taken out of the fabric (Fig. 5a). The gauge length was 200 mm and the strain rate was 2.0 mm/min. Because yarn breakage is not considered, the linear part of the curves is shown. The stiffness of the yarns taken from Fabric A is lower than the yarns out of Fabric B, probably due to remaining crimp, as shown in Fig. 5a. Note a small nonlinearity of the Fabric A curve, absent in the Fabric B case. This feature is not relevant to the tensile deformation of small segments of the yarn. Because of that the theoretical value of 108.5 kN for the yarn stiffness was adopted for yarns in Fabric A and Fabric B.

**Compressive** parameters were defined by compression test on single yarn [36,37]. Fig. 5b shows the test results of compression testing on yarns from each fabric. The length of the compressed yarn (diameter of the compressive platen) was 70 mm. The non-spread yarns from Fabric A were much more easily compressed than the thin and flat spread yarns from Fabric B. The compression parameters for meso-scale simulation were identified by curve fitting to stress-strain curve which were converted from compressive force – thickness curve, the resulting parameters shown in Table 2. The difference in compressibility of the yarns between the two fabrics is reflected in the compressive stiffness  $K_{comp}$ .

**The distortion** invariant  $I_{dist}$  measures the change of angle of the basis vectors in the transverse section of the yarns. The distortion parameters are difficult to identify directly. Because transverse compression involves yarn distortion, it is possible to identify the distortion parameters by inverse identification based on a fabric compression test. This was done with simulation of the fabric deformation in an FE model and finding the parameters reproducing the test results in the best. With the compression behaviour of the yarns identified, the transverse compression diagram of the fabric is fitted by variation of the distortion parameters. Elongation and longitudinal shear of the yarns was neglected. The process is illustrated in Fig. 5c, and the resulting parameters shown in Table 2.

**Longitudinal shear** parameters were also defined using inverse identification based on uniaxial tensile testing on fabrics (Fig. 5d). The load-displacement diagrams up to 50-N load for Fabric A and Fabric B are shown in Fig. 4d. The initial behaviour of a woven fabric under

tension test is nonlinear due to yarn crimp in the fabric. Naturally the nonlinear range of Fabric A with large crimp in the tensile test is wider than that of Fabric B with small crimp. Assuming the adopted parameters for the elongation, the longitudinal shear parameters for the yarn were identified by fitting the results of ABAQUS/Explicit simulation of the uniaxial tension test to the experimental load-elongation diagram of the fabric. The process is illustrated in Fig. 5d, and the resulting parameters shown in Table 2.

**Friction coefficient** for the yarns was set as 0.2, following [38].

#### 4. Results and discussion: Macro-simulation of draping

The macro-draping simulation used boundary conditions, which represent the actual interaction of the acrylic plate, the fabric and the mould (Fig. 6a). The macro-simulation for the homogenised fabric model exhibited a distribution of shear angle over the fabric and the development of wrinkles around the mould (Fig. 6b–e).

The following features can be noted in the macro-simulation for the hemispherical and box moulds.

Fig. 6b, c show macro draping simulation results of Fabric A and B on the hemispherical mould. Both fabrics can follow the mould curved shape and be formed without wrinkles. The maximum shear angle on the mould surface, close to the base of the hemisphere, reaches relatively high values at the final draping position of 43.5° for Fabric A and 47.2° for Fabric B. In spite of these high values, there are no wrinkles on the mould surface. The out-of-plane deformations of the blank outside the hemisphere are slightly larger for Fabric B than for Fabric A, which probably is explained by lower bending rigidity of Fabric B.

For the hemispherical mould, the qualitative features of the draping and the shear angles on the mould surface correspond well to the experimental observations. The final shape of the blank and wrinkling pattern off the mould are quite close for fabrics A and B and do not point to differences in the local distortions for the two fabrics, as discussed above and shown in see Fig. 2a.

Fig. 6d, e show macro draping simulation results of Fabric A and B on the hemispherical mould. At the 10-mm and the final draping positions wrinkles are seen on the corners with small (10 mm and 20 mm) radii for the both fabrics; these wrinkles for Fabric B are smaller and more numerous than for Fabric A. The wrinkles can indicate a potential for local distortions, but macro-simulations do not capture on one hand, conformity of Fabric A to the corners, and on the other hand, local distortions of Fabric B at the corners seen in experiments (Fig. 2b). The simulated wrinkles on the corners were not stable when the element size was changed. This instability can be interpreted as an indication of a behaviour that is not representable by the macro simulation and the

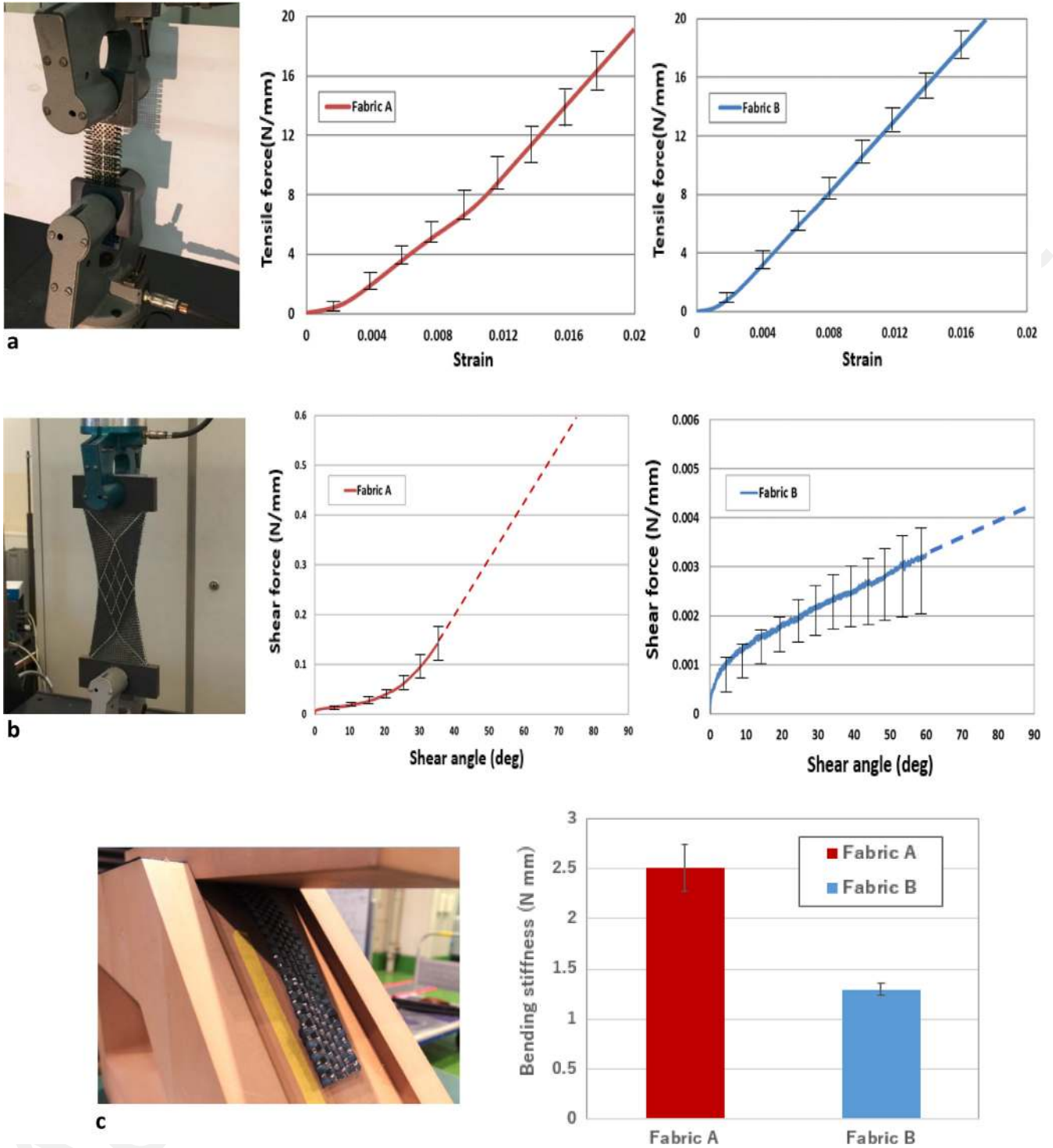


Fig. 4. Identification of the constitutive model of the fabrics, the error bars show scatter (min to max) of the curves: (a) fabric tension; (b) bias extension (the dashed lines show extrapolation of the measured curves); (c) bending. (For interpretation of the references to colour in this figure legend, the reader is referred to the web version of this article.)

need for detailed meso-modelling.



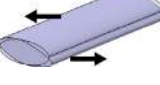

As a trial exercise, a large-scale meso-model for Fabric A was calculated. The result is depicted in Fig. 7a. This calculation took over 10 days of calculation (computer with four CPUs Xeon E5-2690v4, 2.6 GHz and memory size of 16 GB), which clearly prohibits the practical use of such models. It, however, provides a reference case for the macro- and MMZ-simulation.

In the large meso-scale simulation for Fabric A, small wrinkles appear, which are not predicted in the macro-scale simulation (Fig. 7b).

These slight misalignments or small wrinkles in the region of the highest shear near the base of the hemisphere are of the scale of the yarn cross section size and are not seen clearly during the experiment, as they affect only the shapes of the yarn surface, which is difficult to see without cross sectioning.

Fig. 7c, d compare the results of macro-draping and large meso-draping simulation for Fabric A on the hemispherical mould. Fig. 7c depicts vertical positions on the wrinkled outer portion of the blank, and Fig. 7d shows shear angles on the mould at the 10-mm position

**Table 2**  
Parameters of the constitutive model for the yarns.

Deformation mode	Physical invariant and the corresponding potential	Identification test	Identified parameters		
			Parameter	Fabric A	Fabric B
Elongation 	$I_{elong} = \frac{1}{2} \ln(I_4)$ $w_{elong}(I_{elong}) = \frac{1}{2} K_{elong} I_{elong}^2$	Yarn tension, stiffness defined as stiffness of the fibres	$K_{elong}$ , kN	108.5	108.5
Compression 	$I_{comp} = \frac{1}{4} \ln\left(\frac{I_3}{I_4}\right)$ $w_{comp}(I_{comp}) = \begin{cases} K_{comp}  I_{comp} ^p \\ 0 & \text{if } I_{comp} > 0 \end{cases}$	Yarn compression, direct curve fitting	$K_{comp}$ , MPa $p_{comp}$	0.87 1.20	1.25 1.84
Distortion 	$I_{dist} = \frac{1}{2} \ln\left( \frac{\frac{I_1 I_4 - I_5}{2\sqrt{I_3 I_4}}}{\sqrt{\left(\frac{I_1 I_4 - I_5}{2\sqrt{I_3 I_4}}\right)^2 - 1}} \right)$ $w_{dist}(I_{dist}) = \frac{1}{2} K_{dist} I_{dist}^2$	Fabric compression, inverse parameters fit of the compression diagram	$K_{dist}$ , MPa	0.6	0.6
Shear 	$I_{cis} = \sqrt{\frac{I_5}{I_4}} - 1$ $w_{cis}(I_{cis}) = \frac{1}{2} K_{cis} I_{cis}^2$	Fabric uniaxial tension, inverse parameters fit of the force-displacement diagram	$K_{sh}$ , MPa	5	2

**Table 3**  
Calculation cost, hemispherical mould.

Type of simulation	Total CPU time	
	Fabric A	Fabric B
Macro scale	36 min	31 min
Large meso scale	258 h	No convergence
MMZ	44 h	15 h

from mould surface.

Clear wrinkles which occurred in the outer portion of the blank can be seen in both macro-draping and large meso-draping simulation results (Fig. 7c). In macro-draping and large meso-draping simulation, the wrinkles are essentially the same profile. Large meso-draping predicts almost no wrinkle near 0° and 90° directions of the blank (points 0 mm and 220 mm of the profile); macro-draping shows a wrinkle of about 3 mm depth at these points. Experimental observations (Fig. 2a) agree better with the large-scale meso-draping.

Fig. 7d shows the comparison of shear angle distribution along a path on the mould in macro-draping and large meso-draping. There is no significant difference in the profiles; large-scale meso-draping predicts shear angles in the most deformed region higher by about 3°, and more symmetric curve (hence closer to expected fully symmetrical solution). The latter points to good stability of the meso-scale simulations.

These comparisons, apart from pointing out the additional features of deformation predicted by large-scale meso-draping model, show that the macro-draping simulation can be used for extraction of boundary conditions for MMZ modelling.

## 5. Results and discussion: Macro-meso zoom simulation of draping

The meso-calculations used the boundary conditions obtained from the macro-calculations. The displacements along the edge of the meso-“patch”, were extracted from the macro-calculation results along the path corresponding to the edge. The yarns in the meso-calculation are also under contact conditions with the mould and the acrylic plate.

### 5.1. Computational resources

To compare calculation cost of the macro-, large scale meso- and MMZ-draping simulations, the calculations in the same computing configuration were done for Fabrics A and B on the hemispherical mould: computer with four CPUs (Xeon E5-2690v4: 2.6 GHz) and memory size of 16 GB. Table 3 shows the comparison of total CPU time among the calculation cases. In all cases 10 times mass scaling was used.

The macro-scale simulation takes 36 min for Fabric A and 31 min for Fabric B (both models have the same number of elements). Large meso-scale simulation for Fabric A took around 11 days (the same computing configuration), which is prohibitive for practical purposes, and did not converge for Fabric B.

It took around 44 h (2 days, 1/6 of the large scale meso-draping time) to complete the MMZ simulation for Fabric A and 15 h for Fabric B. The size of meso-patch for Fabric A and B was almost same (around 80 mm × 80 mm), but the number of elements for Fabric B was much smaller than that of Fabric A, because of the rougher woven structure of Fabric B. This lower number of elements explains the smaller calculation time for Fabric B. These times are still considerable, but tolerable (as proclaimed by draping technology designers) for investigation of “problem” locations on the mould.

In the present research we did not investigate how the calculation time would change with change of the computing configuration, for example, with the number of CPUs. This is the subject of the on-going work.

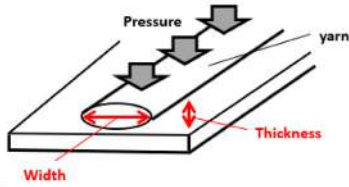
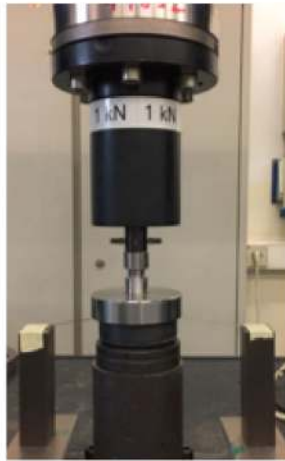
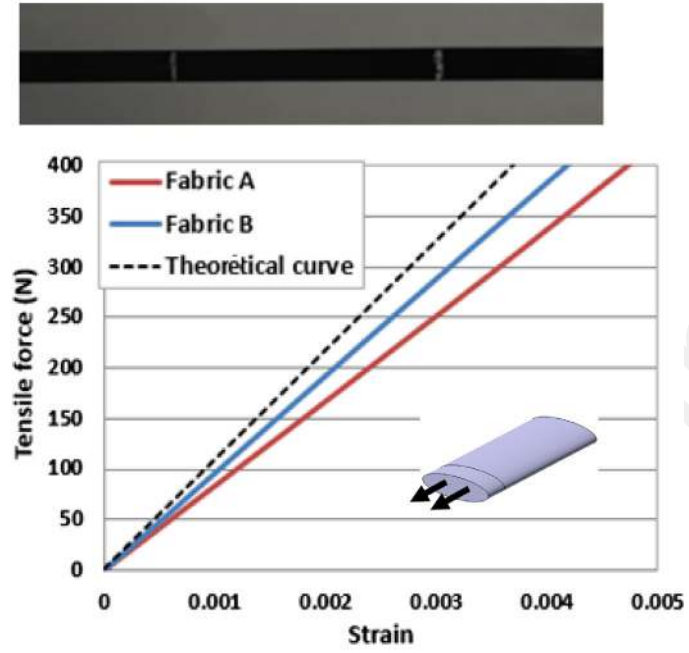
### 5.2. MMZ, hemispherical mould

Fig. 8 shows results of MMZ simulations of the fabrics draping on the hemispherical mould (the meso-region shown in Fig. 8a, calculated meso-deformation in Fig. 8d, e) in comparison with the experimentally-observed configurations (Fig. 8b, c). The MMZ simulation for Fabric A (Fig. 8d) shows no local yarn buckling or other distortions. This result corresponds well with the experimental observation (Fig. 8b) and is the same behaviour as seen in large-scale meso-simulations. MMZ simulation for Fabric B (Fig. 8e) shows yarn buckling with the same pattern as observed in the experiment (Fig. 8c). As in the experiment, the buckling happens in the low-shear-angle zone of the draped fabric. Note that when macro-draping simulations are performed in a simple kinematic





a



b

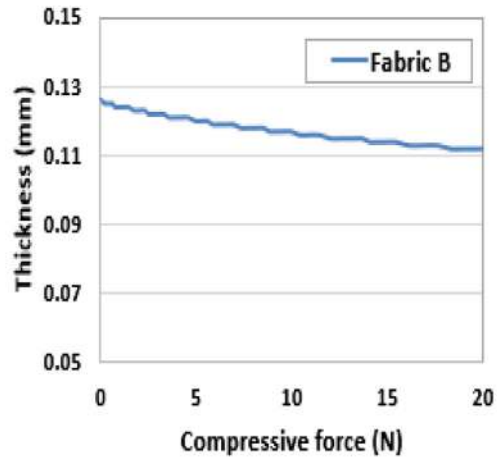
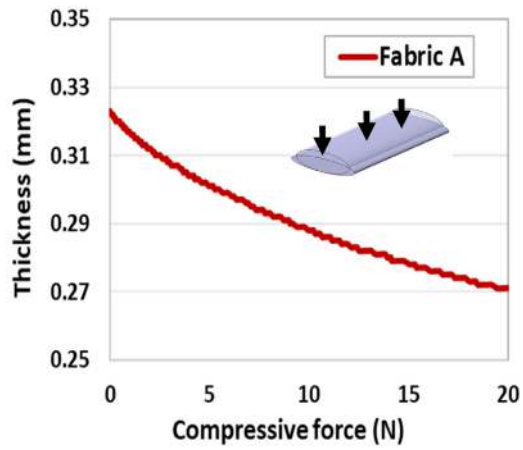
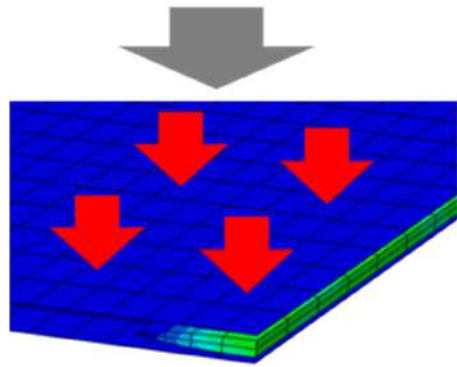
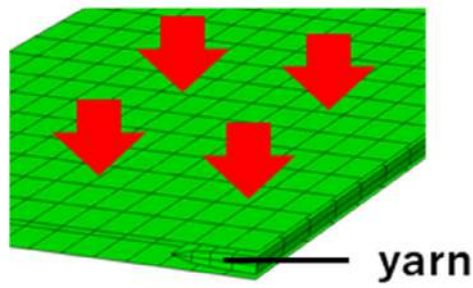
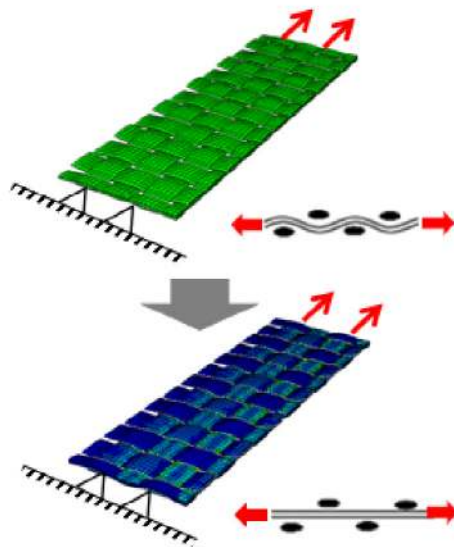
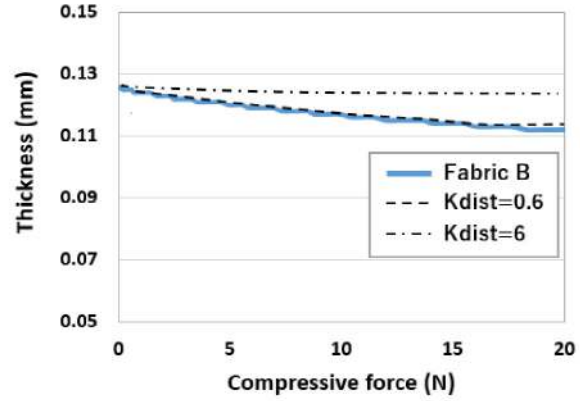
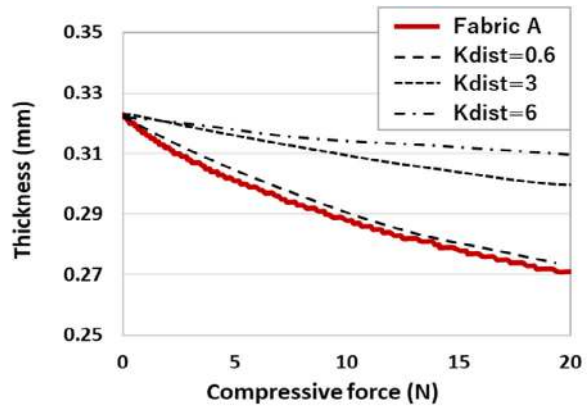


Fig. 5. Identification of the constitutive model of the yarns: (a) yarn tension; (b) yarn compression; (c) fabric compression, fit for the yarn distortion model; (d) fabric uniaxial tension, fit for the yarn longitudinal shear model. Average curves are shown. (For interpretation of the references to colour in this figure legend, the reader is referred to the web version of this article.)



c



d

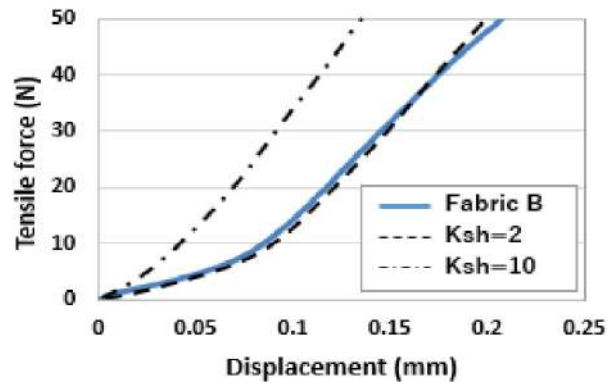
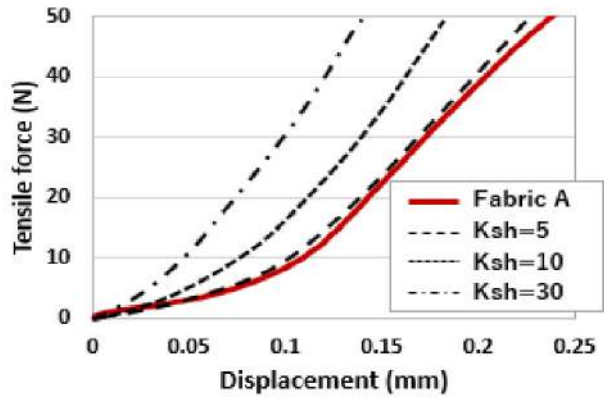


Fig. 5. (continued)

modelling only the high-shear-angle regions attract attention, as the places where wrinkles are likely to appear.

In more elaborate mechanical FE simulations, the wrinkles, the tensions in the yarns, and all mechanical quantities (of a continuous

model) can be analysed. However, the draping is represented by the fabric mid-surface. The MMZ simulation represent all effects of yarn constraint during the draping (discussed in Section 2).

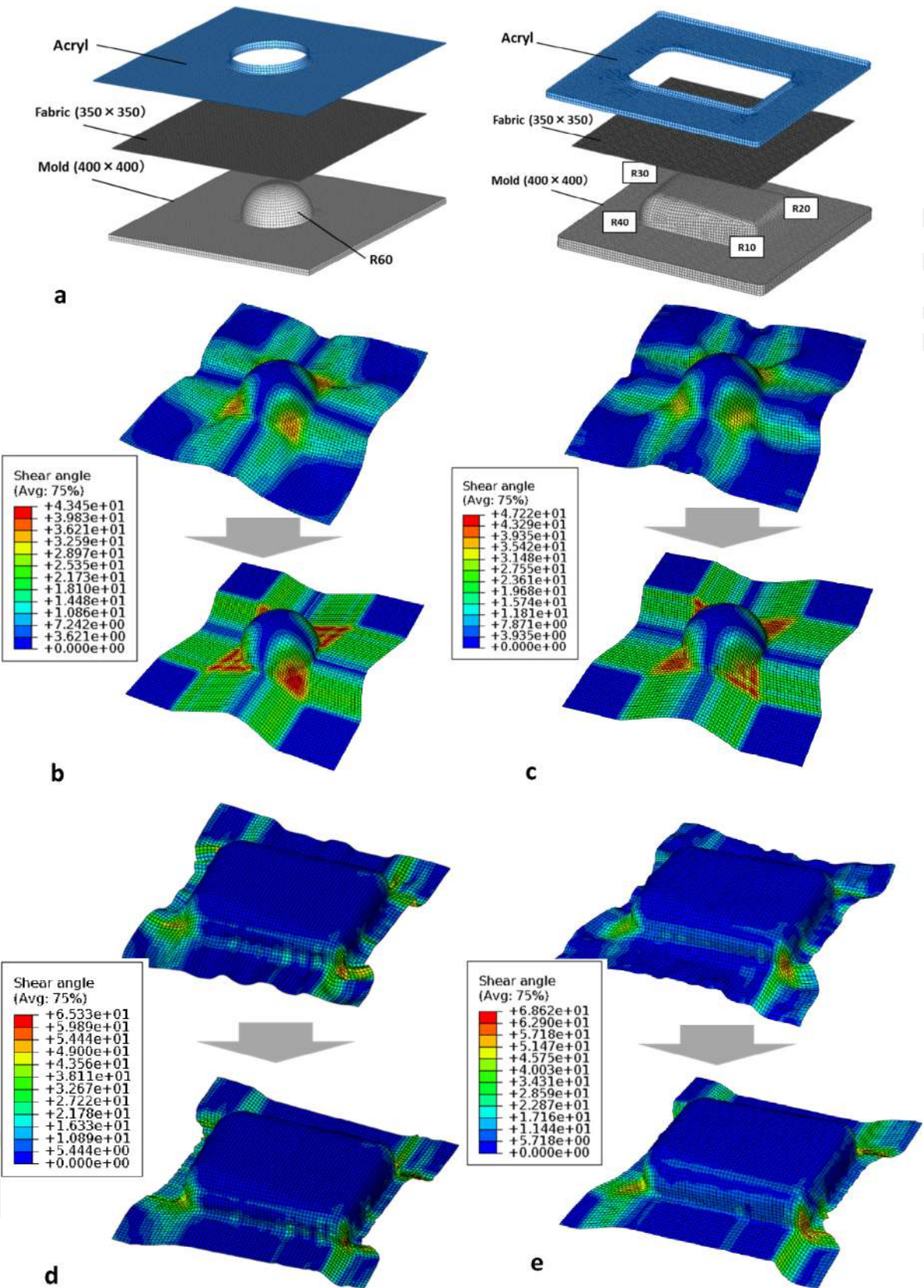


Fig. 6. Macro-simulation setup: FE model configuration for the hemispherical and the box moulds (a); two stages of the fabric deformation on the hemispherical and box moulds, Fabric A (b, d) and Fabric B (c, e): acrylic plate moves 10 mm down from the mould top and the final position. Several highly distorted elements (shear angle over 85°) are excluded from the plot (d). (For interpretation of the references to colour in this figure legend, the reader is referred to the web version of this article.)

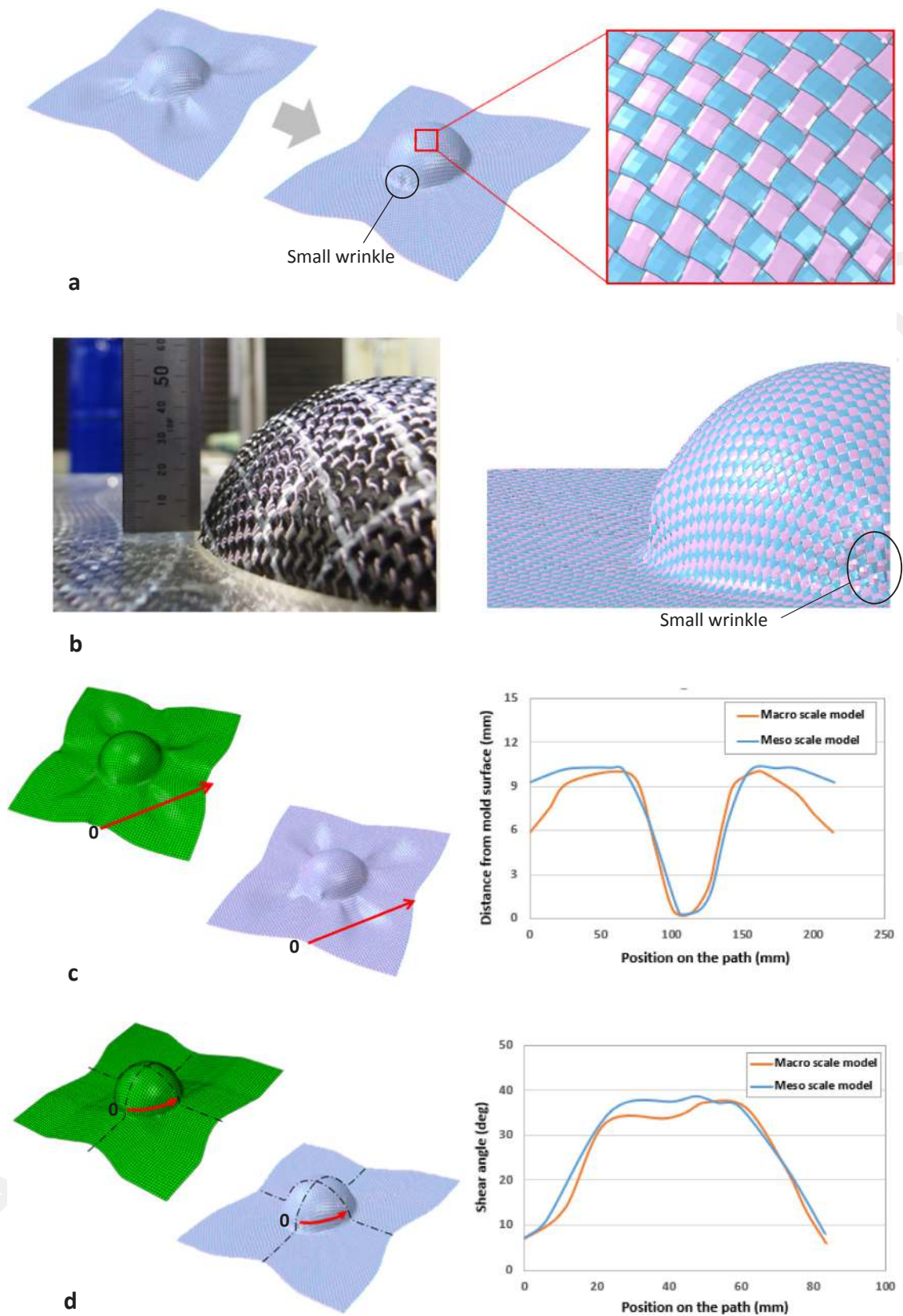
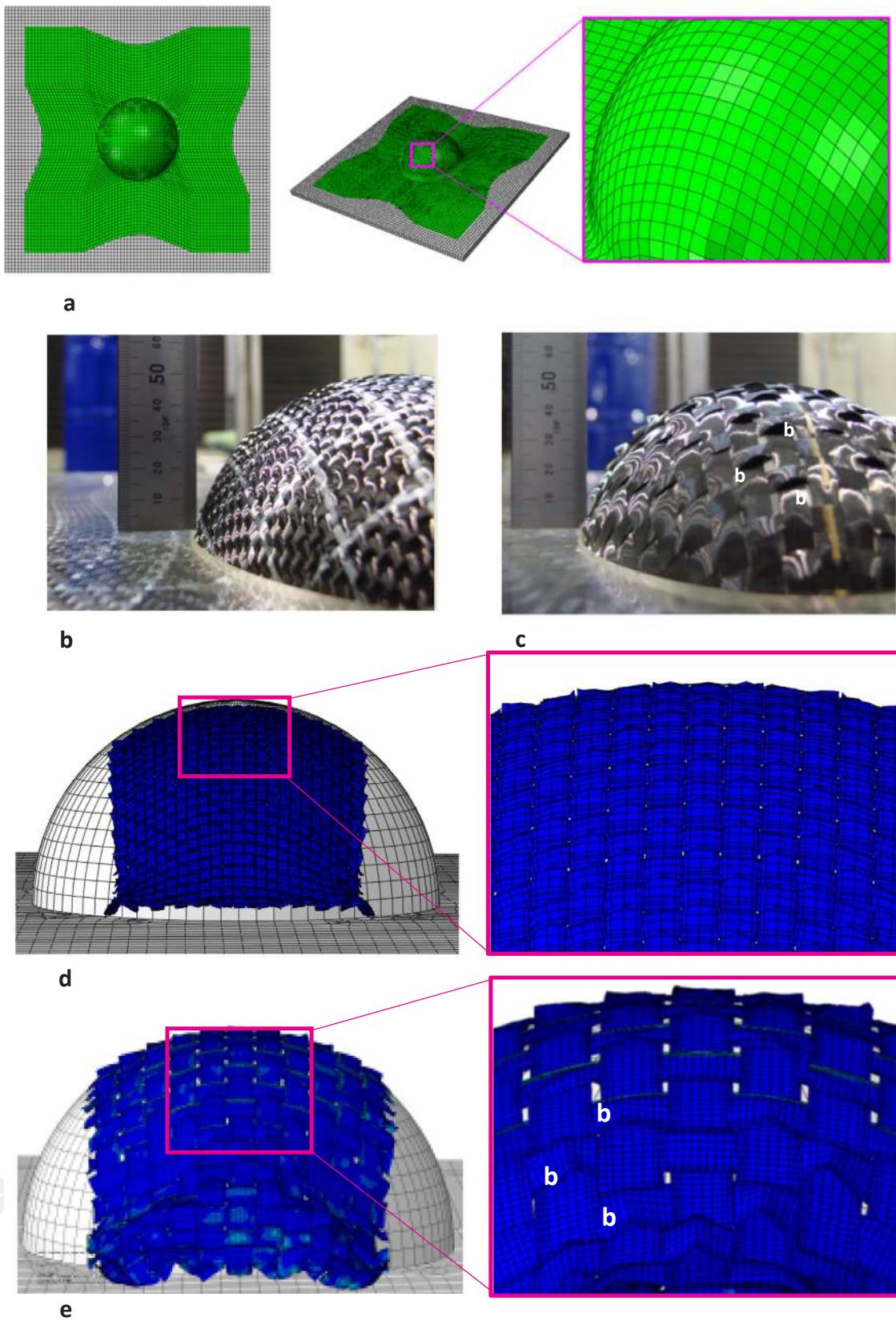
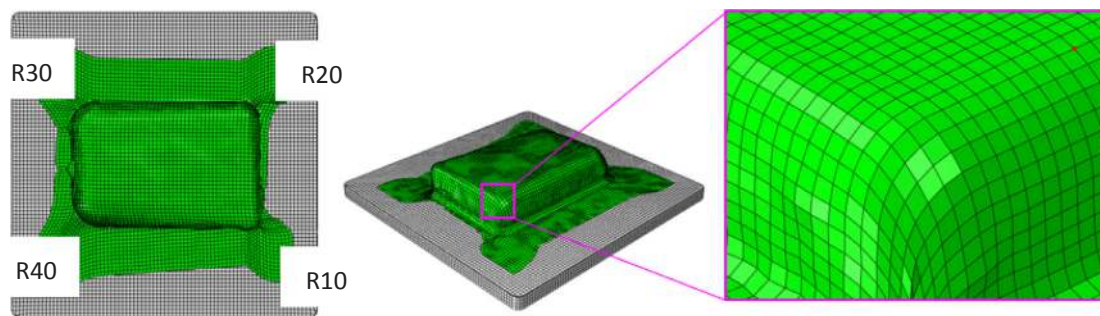


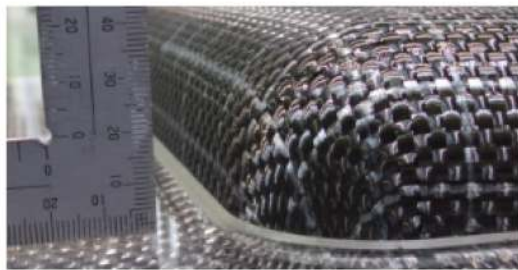
Fig. 7. Large scale meso-simulation, Fabric A on hemispherical mould: (a) a general view of the draped fabric; (b) zoom-in of the region around hemisphere, (c) Comparison of wrinkle profiles (d) Comparison of the distribution of shear angle. (For interpretation of the references to colour in this figure legend, the reader is referred to the web version of this article.)



**Fig. 8.** MMZ simulations for the hemispherical mould in comparison with the experimental draping: (a) the meso-zoom region; test results, Fabric A (b) and B (c); meso-zoom simulation, Fabric A (d) and Fabric B (e). (For interpretation of the references to colour in this figure legend, the reader is referred to the web version of this article.)



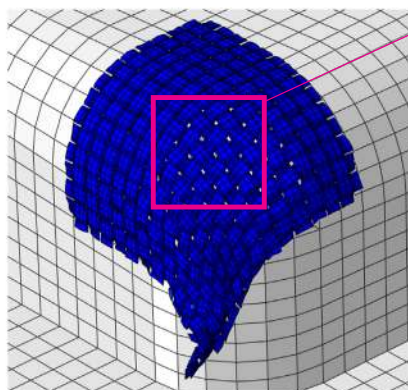
a



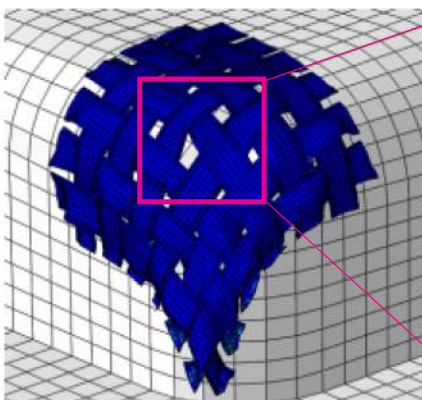
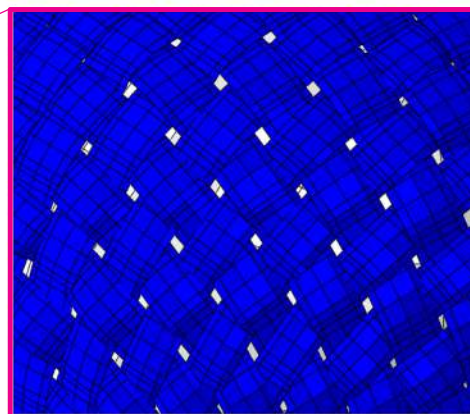
b



c



d



e

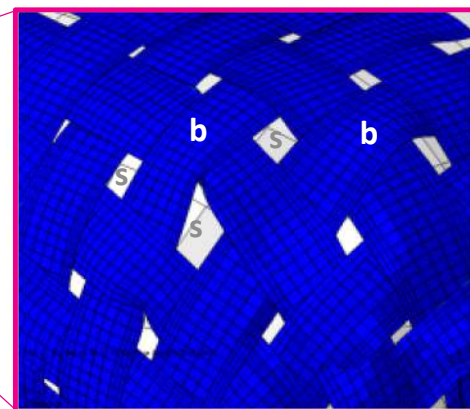


Fig. 9. MMZ simulations for the box mould in comparison with the experimental draping: (a) the meso-zoom region; test results, Fabric A (b) and B (c); meso-zoom simulation, Fabric A (d) and Fabric B (e). (For interpretation of the references to colour in this figure legend, the reader is referred to the web version of this article.)

### 5.3. Box mould

Fig. 9 shows results of the MMZ simulations of the fabrics draping on the box mould in comparison with the experimentally-observed

configurations. The MMZ region is defined in the corner of the box with the radius of 20 mm.

The MMZ models show the same defect patterns as in the experiment. There are two types of defects: yarn buckling and yarn slippage,

both much more prominent for Fabric B.

The buckling is caused by the same lateral constraints for yarn deformation as were discussed for the hemispherical mould in the previous section. It is almost not seen for Fabric A, however, certain distortion of the yarns are noticeable in Fig. 9d. For Fabric B, buckling is evident in the experiment (Fig. 9c) and the calculations (Fig. 9e); the positions of yarn buckling in the experiment and the calculations are the same.

The yarn slippage is a result of high local draping deflection of the fabric on a corner with a small radius of curvature of 20 mm. This radius is comparable with the dimensions of the yarns; local increase of the draped surface of the fabric forces the yarns to move away one from another. Gaps between the yarn are seen even for Fabric A (Fig. 9d); however, high crimp and connectivity of the yarns in this Fabric and tighter placement of the yarns prevent slippage. On the contrary, for Fabric B the gaps are large (Fig. 9e), as they were in experiment (Fig. 9c): low crimp and flat yarn shape allow “sliding” on a high-curvature mould corner. With the correct representation of the gaps, the MMZ simulation gives additional (in comparison with the macro-simulation) information on the change (decrease) of local fibre volume fraction in the preform.

## 6. Conclusions

The feasibility and usefulness of the macro-meso zoom (MMZ) simulations of the woven fabric draping were demonstrated. The MMZ calculations reveal the characteristic features of the yarns local deformations and defects of the draping. These features are not present in macro-calculations by the very nature of the material approximation as a continuous medium. Macro-meso coupling allowed incorporation of the local features in the full-scale forming simulation. MMZ models of both the hemispherical and box moulds draping represent well (1) the differences in behaviour of Fabric A (high crimp, high areal density, thick yarns) and Fabric B (low crimp, lower areal density, spread yarns), hence is sensitive to the details of the fabric construction and (2) localisation and character of yarn buckling and slippage, hence is sensitive to local details of the yarn deformation.

In general, MMZ simulations:

- represent local features of the fabric deformation, e.g. yarn buckling and yarn slippage, which would create a defect in the composite part after impregnation and consolidation;
- allow estimation of the change of the local fibre volume fraction of the preform due to the slippage and change of the yarn shapes and fibre directions due to the buckling;
- calculate these additional draping features on a computational cost which is not prohibitive for practical calculations and is several times smaller than that of large scale meso-calculations.

## Acknowledgements

The work reported here was funded by the Toray Group and was done in the framework of the Toray Chair on Composite Materials at KU Leuven, held by S.V. Lomov.

## References

- [1] Boisse P, Colmar J, Hamila N, Naouar N, Steer Q. Bending and wrinkling of composite fiber preforms and prepregs. A review and new developments. *Composites Part B* 2018;141:234–49.
- [2] Peng X, Cao J. A dual homogenisation and finite element approach for material characterisation of textile composites. *Composites Part B* 2002;33:45–56.
- [3] Lomov SV, Ivanov DS, Verpoest I, Zako M, Kurashiki T, Nakai H, et al. Meso-FE modelling of textile composites: road map, data flow and algorithms. *Compos Sci Technol* 2007;67:1870–91.
- [4] Badel P, Vidal-Salle E, Maire E, Boisse P. Simulation and tomography analysis of textile composite reinforcement deformation at the mesoscopic scale. *Compos Sci Technol* 2008;68(12):2433–40.
- [5] Creech G, Pickett AK. Meso-modelling of non-crimp fabric composites for coupled drape and failure analysis. *J Mater Sci* 2006;41(20):6725–36.
- [6] Sirtautas J, Pickett AK, Lepicier P. A mesoscopic model for coupled drape-infusion simulation of biaxial non-crimp fabric. *Compos Part B – Eng* 2013;47:48–57.
- [7] Pickett AK, Sirtautas J, Erber A. Braiding simulation and prediction of mechanical properties. *Appl Compos Mater* 2009;16(6):345–64.
- [8] Gatouillat S, Bareggi A, Vidal-Salle E, Boisse P. Meso modelling for composite preform shaping – simulation of the loss of cohesion of the woven fibre network. *Composites Part A* 2013;54:135–44.
- [9] Dureisseix D, Farhat C. A numerically scalable domain decomposition method for the solution of frictionless contact problems. *Int J Numer Meth Eng* 2001;50(12):2643–66.
- [10] Dhia HB, Rateau G. The Arlequin method as a flexible engineering design tool. *Int J Numer Meth Eng* 2005;62(11):1442–62.
- [11] Amini AM, Dureisseix D, Cartraud P. Multi-scale domain decomposition method for large-scale structural analysis with a zooming technique: application to plate assembly. *Int J Numer Meth Eng* 2009;79(4):417–43.
- [12] Gendre L, Allix O, Gosselet P. A two-scale approximation of the Schur complement and its use for non-intrusive coupling. *Int J Numer Meth Eng* 2011;87(9):889–905.
- [13] Feyel F. A multilevel finite element method (FE2) to describe the response of highly non-linear structures using generalized continua. *Comput Methods Appl Mech Eng* 2003;192(28–30):3233–44.
- [14] Gupta V, Kim D-J, Duarte CA. Analysis and improvements of global-local enrichments for the generalized finite element method. *Comput Methods Appl Mech Eng* 2012;245-246(Supplement C):47–62.
- [15] Whitcomb JD. Iterative global/local finite element analysis. *Comput Struct* 1991;40(4):1027–31.
- [16] Llorca J, Gonzalez C, Molina-Aldaregui JM, Segurado J, Seltzer R, Sket F, et al. Multiscale modelling of composite materials: a road map towards virtual testing. *Adv Mater* 2011;23:5130–47.
- [17] Sihm S, Kim RY, Kawabe K, Tsai SW. Experimental studies of thin-ply laminated composites. *Compos Sci Technol* 2007;67(6):996–1008.
- [18] Nishii M, Hirashima T, Kurashiki T. Dry fabric forming analysis considering the influence of tensions on in-plane shear behavior. *J Soc Mater Sci, Jpn* 2014;63(5):380–5.
- [19] Nishii M, Hirashima T, Kurashiki T. Textile composite reinforcement forming analysis considering out-of-plane bending stiffness and tension dependent in-plane shear behavior. In: 16th European Conference on Composite Materials (ECCM-16), Seville; 2014. p. paper 089.
- [20] Charmentant A, Vidal-Salle E, Boisse P. Hyperelastic modelling for mesoscopic analyses of composite reinforcements. *Compos Sci Technol* 2011;71:1623–31.
- [21] Verpoest I, Lomov SV. Virtual textile composites software Wisetex: integration with micro-mechanical, permeability and structural analysis. *Compos Sci Technol* 2005;65(15–16):2563–74.
- [22] Lomov SV, Verpoest I, Cichosz J, Hahn C, Ivanov DS, Verleye B. Meso-level textile composites simulations: open data exchange and scripting. *J Compos Mater* 2014;48:621–37.
- [23] Truong Chi T, Vettori M, Lomov SV, Verpoest I. Carbon composites based on multiaxial multiply stitched preforms. Part 4: Mechanical properties of composites and damage observation. *Composites Part A* 2005;36:1207–21.
- [24] Mikhalek DS, Truong TC, Borovkov AI, Lomov SV, Verpoest I. Experimental observations and finite element modelling of damage and fracture in carbon/epoxy non-crimp fabric composites. *Eng Fract Mech* 2008;75(9):2751–66.
- [25] Harrison P, Clifford MJ, Long AC, Rudd CD. Constitutive modelling of impregnated continuous fibre reinforced composites Micromechanical approach. *Plast, Rubber Compos* 2002;31(2):76–86.
- [26] Potluri P, Perez Ciurezu DA, Ramgulum RB. Measurement of meso-scale shear deformations for modelling textile composites. *Composites Part A* 2006;37(6):303–14.
- [27] Harrison P, Abdiwi F, Guo Z, Potluri P, Yu WR. Characterising the shear-tension coupling and wrinkling behaviour of woven engineering fabrics. *Composites Part A* 2012;43:903–14.
- [28] Zhu D, Mobasher B, Rajan SD. Dynamic tensile testing of kevlar 49 fabrics. *J Mater Civ Eng* 2011;23(3). s.p.
- [29] Zouari R, Amar SB, Dogui A. Experimental and numerical analyses of fabric off-axes tensile test. *J Text Inst* 2010;101:58–68.
- [30] Launay J, Hivet G, Duong AV, Boisse P. Experimental analysis of the influence of tensions on in plane shear behaviour of woven composite reinforcements. *Compos Sci Technol* 2008;68(2):506–15.
- [31] Grosberg P. The mechanical properties of woven fabrics. Part II The bending of woven fabrics. *Text Res J* 1966;36(3):205–11.
- [32] Lomov SV, Truettzev AV, Cassidy C. A predictive model for the fabric-to-yarn bending stiffness ratio of a plain-woven set fabric. *Text Res J* 2000;70(12):1088–96.
- [33] Boehler JP. Applications of Tensor Functions in Solid Mechanics. CISM Course no. 292. Springer-Verlag; 1987.
- [34] Zheng QS. Theory of representations for tensor functions – a unified invariant approach to constitutive equations. *Appl Mech Rev* 1994;47(11):545–87.
- [35] Charmentant A, Vidal-Salle E, Boisse P. 3D Hyperelastic constitutive model for yarn behaviour description. In: *Material Forming – Esaform 2012, Pts 1 & 2*; 2012. p. 267–72.
- [36] Lomov SV, Gorbatikh L, Houille M, Kotanjac Z, Koissin V, Vallons K, et al. Compression resistance and hysteresis of carbon fibre tows with grown carbon nanotubes/nanofibres. *Compos Sci Technol* 2011;71:1746–53.
- [37] Potluri P, Sagar TV. Compaction modelling of textile preforms for composite structures. *Compos Struct* 2008;86(1–3):177–85.
- [38] Mulvihill DM, Smerdova O, Sutcliffe MPF. Friction of carbon fibre tows. *Compos Part A – Appl Sci Manuf* 2017;93:185–98.